Title
Forms and distribution of Ce in a ferromanganese nodule

Authors
Marcus, Matthew A
Toner, Brandy M
Takahashi, Yoshio

Publication Date
2018-05-01

DOI
10.1016/j.marchem.2018.03.005

Peer reviewed

Marine Chemistry 202 (2018) 58–66

Contents lists available at ScienceDirect

Marine Chemistry

journal homepage: www.elsevier.com/locate/marchem

Forms and distribution of Ce in a ferromanganese nodule

Matthew A. Marcus[a,*], Brandy M. Toner[b], Yoshio Takahashi[c]

[a] Advanced Light Source, Lawrence Berkeley National Laboratory, Berkeley, CA 94720, USA
[b] Department of Soil, Water, and Climate, University of Minnesota, St. Paul, MN 55108, USA
[c] Department of Earth and Planetary Science, Graduate School of Science, The University of Tokyo, Hongo, Bunkyo-ku, Tokyo 113-0033, Japan

ARTICLE INFO

Keywords:
Ferromanganese nodule
Cerium
X-ray spectroscopy
Chemical speciation

ABSTRACT

We studied the distribution and speciation of Ce in a previously-characterized ferromanganese nodule from the South Pacific Gyre using X-ray microspectroscopy.We find Ce in three types of environment – diffusely in all parts of the nodule except the Fe-rich, Mn-poor "matrix", fluorapatite grains with a negative Ce anomaly suggestive of an authigenic origin, and localized spots whose composition is consistent with a pseudobinary mixture of sorbed Ce^{4+} and a mix of sorbed Ce^{3+} and CeO_2. In contrast with some other elements such as Ti, there is no clear correlation of the Ce concentration in the diffuse areas with either that of Mn, Fe or any linear combination of the two.We argue that the CeO_2 came from oxidation of Ce^{3+} in the water column, while the Ce in the Mn-rich regions may have been initially deposited as Ce^{4+} and then partially reduced.

1. Introduction

Rare-earth elements (REE) have drawn much attention from geochemists not only for their economic utility but also for their usefulness in tracing the formation and subsequent evolution of many kinds of rocks and minerals.Among the REE, those which commonly exhibit two or more valence states are particularly interesting because they respond to redox conditions during and after deposition.In particular, Ce is famous for "Ce anomalies", in which its elemental abundance in a particular system is either greater or less expected based on the abundances of other REE (De Baar et al., 1991; Elderfield et al., 1988). These anomalies are, in part, due to the fact that Ce^{3+} can be oxidized to the less-soluble Ce^{4+}.

Ferromanganese nodules are slow-growing, layered mineral deposits with concentric growth patterns which may hold time-resolved records of geochemical conditions over many millions of years (Calvert and Cronan, 1978; Koschinsky and Hein, 2003). These materials contain a number of elements of geochemical interest such as Fe and Mn (major elements), and Cu, Ni, REE, Ti, and V (trace elements) (Bau et al., 2014; Hein et al., 2013; Peacock and Sherman, 2007; Takahashi et al., 2007). Using modern micro-analytical techniques, it is possible to study the abundances and speciation of these elements within specific zones of mineral accumulation (Manceau et al., 2002; Marcus et al., 2015; Marcus et al., 2004).Greater spatial resolution provides effectively greater time resolution, as well as insights into spatial-correlation between trace element speciation and specific mineral phases.If coupled to isotopic age-dating methods and trace element isotope fractionation observations, then a micro-analytical approach can provide the timing of mineral precipitation events, the chemical speciation and isotope signatures of trace element(s) sequestered in those conditions, at least if there has been no diagenetic changes or secondary re-deposition.While micro X-ray absorption spectroscopy cannot be used for trace elements present in concentrations as low as are accessible with some other methods, it does provide speciation and valence data.This method can thus be a useful addition to the suite of analytic methods employed in geochemical studies.While it is currently unusual to obtain all three analytical perspectives for ferromanganese nodules in a single study, the utility of using of two of the three approaches together has been demonstrated for marine mineral deposits (Marcus et al., 2015; Toner et al., 2016).

In a previous paper, we described in detail the growth rate (^{10}Be), mineralogy and stable isotope composition of the major element Fe, and speciation of trace elements Ti and V for a hydrogenetic ferromanganese nodule from the South Pacific Gyre (Marcus et al., 2015). In this manuscript, we return to that nodule and concentrate on the speciation and spatial distribution of Ce.We find that, although the nodule grew in an oxic environment and is mostly composed of oxidized forms of Fe^{3+} and Mn^{4+}, it contains Ce in the reduced, 3+ state as well as sorbed Ce^{4+} and $Ce^{4+}O_2$.Further, the distribution of Ce breaks down into three patterns, each characterized by differing speciation.We find mixed Ce^{3+}/Ce^{4+} disseminated throughout most of the nodule, CeO_2-rich spots, and apatite ($Ca_5(PO_4)_3X$, X = F, Cl, OH) crystals containing Ce^{3+} and Ce^{4+}.These observations are surprising in the light of previous work on Ce in ferromanganese nodules in which only Ce^{4+} was

* Corresponding author.
E-mail address: mamarcus@lbl.gov (M.A. Marcus).

https://doi.org/10.1016/j.marchem.2018.03.005
Received 1 September 2017; Received in revised form 19 March 2018; Accepted 22 March 2018
Available online 27 March 2018
0304-4203/ Published by Elsevier B.V.

found (Takahashi et al., 2007; Takahashi et al., 2002). In that previous work, it was suggested that the Ce either sorbed onto Mn, a process which they showed was accompanied by oxidation of Ce^{3+} to Ce^{4+} or adhesion of Ce^{4+}-bearing particles, presumably CeO_2.However, their work was done with a "macro" (~1 mm) beam.We show that the use of a micro beam reveals much more complexity than had been previously found.We will describe the nodule and our findings regarding Ce and suggest some interpretations of what we find.

2. Nodule description and methods

Since the nodule was described in (Marcus et al., 2015), we will only summarize its provenance and basic properties here.The nodule came from a site, South Pacific Gyre-2, at 26°03.090′S, 156°53.650′W, at 5126 m water depth.This site is located in a region of abyssal hill topography, with several small seamounts scattered about the region.The coring site is located within magnetic polarity Chron 34n, so the crustal age may range from 84 to 124.6 Ma (Gradstein and Ogg, 2002). Based on a tectonic reconstruction of the region (Larson et al., 2002), the crust was accreted along the Pacific-Phoenix spreading center ~95 Ma ago at ultra-fast spreading rates (~90 km/Ma, half-rate).The water column overlying the site is one known to be of low primary productivity.

A polished petrographic thin section of the nodule was prepared by Spectrum Petrographics, Inc. The nodule was embedded in 3 M Scotchcast #3, mounted on a fused silica slide with Loctite Impruv 363 adhesive, and sectioned to a 30 µm slice with a diamond-polished electron-microprobe finish.$^{10}Be/^{9}Be$ analysis was used to derive a growth rate of (3.8–4.2) ± 0.7 mm/Ma.

Following the notation of (Marcus et al., 2015), we define "inner" and "outer" regions of the nodule which show differing morphology and Fe/Mn ratios.The "inner" zone contains the oldest material, while the "outer" is close to the surface and more recently deposited.While both zones show botryoidal morphologies with an Fe-rich, Mn-poor "matrix" between botryoids, the inner zone is conspicuously richer in matrix and has a higher Fe/Mn ratio in the botryoids than the outer zone.

X-ray fluorescence (XRF) maps and XANES (X-ray absorption near-edge structure) spectroscopy were done on Beamline 10.3.2 at the Advanced Light Source.The pixel size of the maps ranged from 7 to 20 µm.In order to understand the patterns of occurrence of Ce species, we performed chemical-state mapping by doing XRF at energies of 5715.0, 5725.5, 5728.35, 5731.5 and 5746.0 eV and a pixel size of 7 µm.In order to reduce any effects of sample drift during mapping, we took the maps in such a way that each scan line was taken at each energy before moving to the next line.This mode is in contrast with the older procedure of taking the whole map at one energy, then taking it again at the next, etc.The lowest-energy maps were used to image the distributions of Ti, Ca and, for some regions, Cl.Additional maps were taken on the same areas at 10 keV, in order to see the distributions of Mn, Fe, Ni and Cu.These maps were taken separately from the chemical-state maps because the strong signals from Fe and Mn made it necessary to narrow the entrance slit in order to avoid saturating the detector.The maps were registered together using Ti (seen in both chemical-state and 10 keV maps) as a fiducial.In addition to fitting the Ce signals at the various energies of the chemical maps to read off the amounts of Ce^{3+}, Ce^{4+} and CeO_2, we also derived the total Ce amount by taking the difference between the Ce signals at 5746 eV and 5715 eV.Differencing was needed because the background from V, Ti and Ba often exceeded the signal from Ce.The upper energy was chosen because the signals from our three reference materials are equal at that energy, as shown in Fig. 1.Energy calibration was done using CeO_2 as a standard (first peak at 5730.39 eV; peak for Ce^{3+}-doped YAG at 5725.88 eV).These maps were interpreted using as references Ce^{4+}-sorbed δ-MnO_2 (Takahashi et al., 2000), Ce-sorbed ferrihydrite and CeO_2.

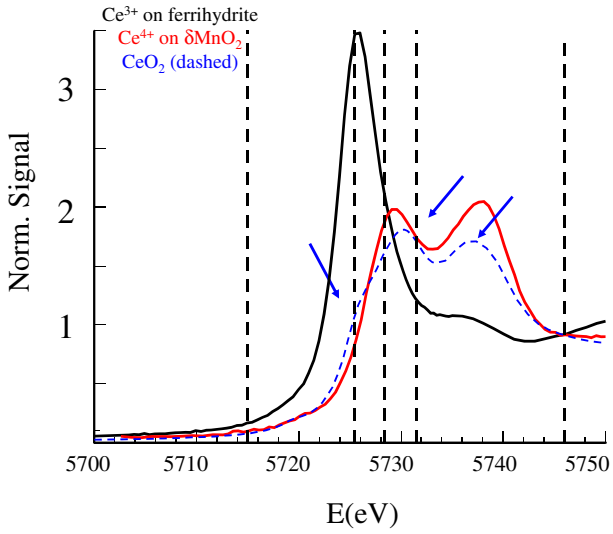

Fig. 1. XANES spectra of standards.The vertical lines show the energies used in chemical-state mapping. Arrowed features show the distinction between sorbed Ce^{4+} and CeO_2.

The reason for using both Ce-sorbed MnO_2 and CeO_2 as Ce^{4+} references is that the XANES of CeO_2 has distinct features not found in spectra from, for instance, sorbed Ce^{4+}.Our reference spectra are shown in Fig. 1.The shoulder on the left side of the first peak and the shift of the peak positions relative to those of sorbed Ce^{4+} may be seen.The reasons for the differences between the XANES of fluorite-structure (8-coordinate) CeO_2 and other, octahedral, Ce^{4+} species have ascribed to many-body effects by (Kaindl et al., 1988; Soldatov et al., 1994). The same reference spectra were used in linear-combination fitting of spot XANES spectra from the sample.

La, Ce and Pr concentrations in Ca-rich (apatite) grains were measured by taking XRF spectra at energies of 5470 eV, 5500 eV, 5715 eV, 5746 eV, 5940 eV and 6000 eV, energies chosen to cross the L_3 edges of La, Ce and Pr.The below-edge spectra were subtracted from the above-edge spectra and then fitted using parameters derived from measurements on spectra taken on a geological fluorapatite sample (Yates Mine, Otter Lake, Ontario Canada).This sample was characterized by electron microprobe and its composition was similar to that published for a sample from the same locality (Yang et al., 2014). Cerium anomaly ratios were defined as

$$r = [Ce]/\sqrt{[La][Pr]}$$
$$\text{Anomaly} = \log\left(\frac{r}{r_{CI}}\right) \quad (1)$$

where CI refers to chondritic abundances (Anders and Grevesse, 1989).

3. Results

3.1. Cerium distribution

Figs. 2 and 3 show maps of the distribution of Ce compared with those of Mn and Fe in Inner and Outer regions of the nodule.Consistent with previous work, there are botryoidal regions of mixed Mn and Fe, displaying rhythmic oscillations of density and Ni-rich "streaks", and an Fe-rich "matrix" between botryoids (Marcus et al., 2015). The dash-

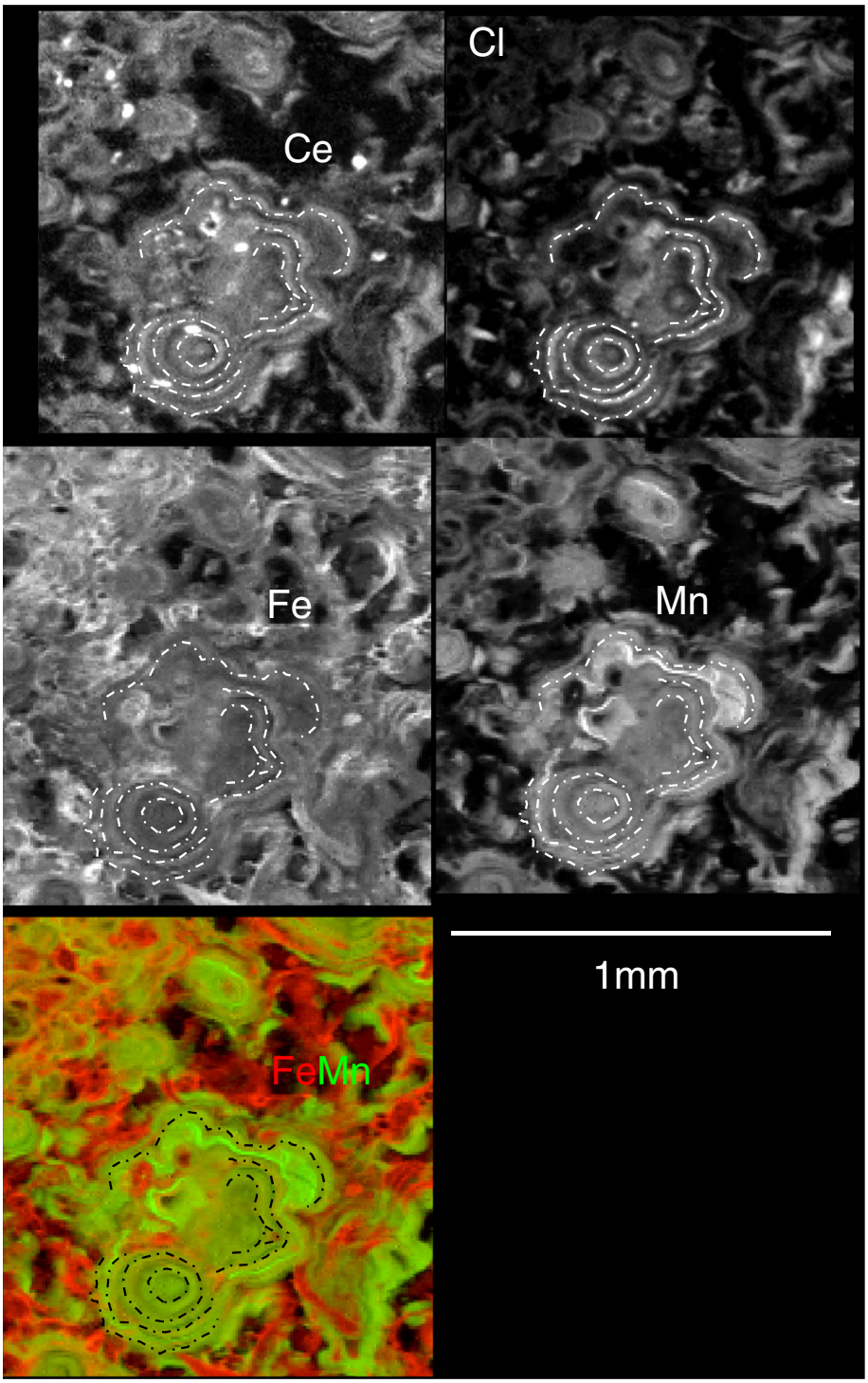

Fig. 2. XRF maps of Ce, Fe, Mn and Cl in the Inner region.White signifies higher concentrations, black lower.The dash-dotted lines are guides to the eye, tracking the banding in the botryoids and are drawn to match the maxima in Cl, which is a proxy for porosity.In the bottom panel, Fe is coded as red, Mn as green. (For interpretation of the references to colour in this figure legend, the reader is referred to the web version of this article.)

dotted curves in these figures are guides for the eye, showing corresponding bands in each image.The most obvious feature of the Ce maps is that there is little or no Ce in the Fe-rich matrix.A possible reason for this lack will be discussed below.

Both Ce maps also show localized accumulations of Ce not mirrored by any feature of the distribution of any other elements mapped.In the Outer map (Fig. 3), some of these line up with (Fe, Mn) minima as shown by the dot-dashed curves, but no such correspondence is visible in Fig. 2.

In Fig. 2, the map for Cl is shown and XANES for this element is consistent with its occurrence as inorganic chloride (presumably dried porewater), outer-sphere sorbed inorganic chloride (likely sorbed from

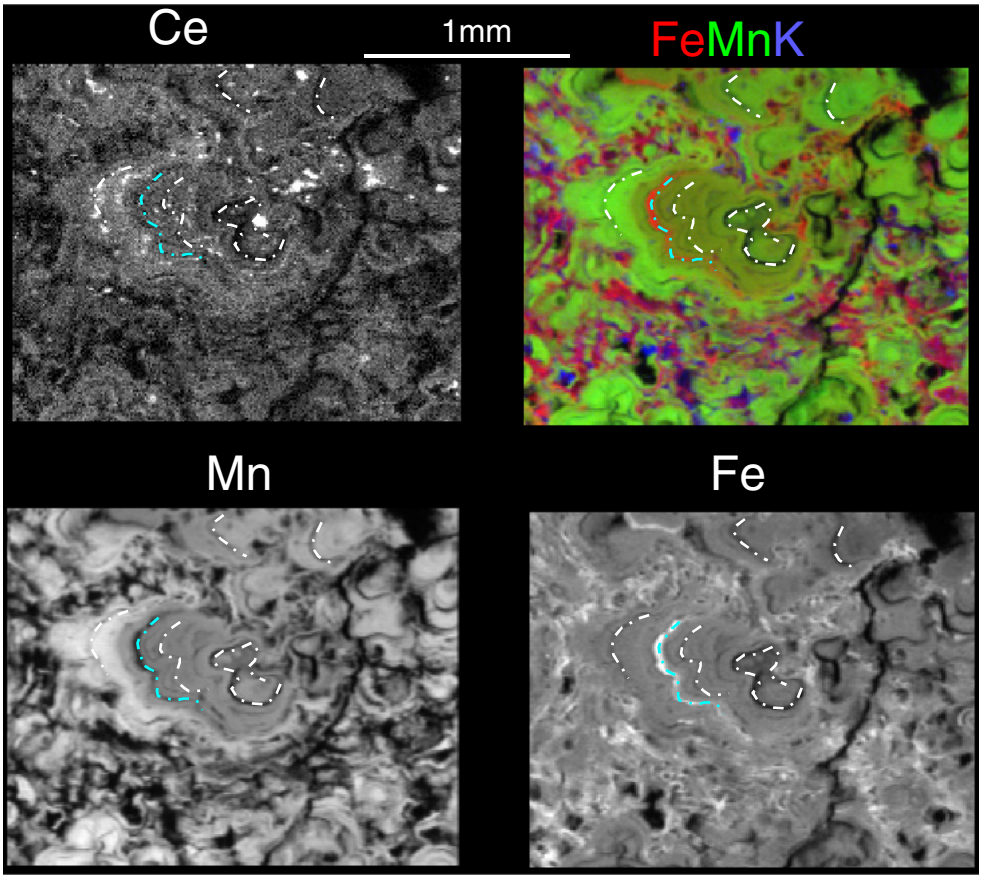

Fig. 3. Maps of Ce, Mn and Fe for an Outer region.In the colour map, Fe, Mn and K are coded red, green and blue, respectively.The white dot-dashed curves mark low-(Mn,Fe) arcs; the cyan curve marks a streak of high Fe content. (For interpretation of the references to colour in this figure legend, the reader is referred to the web version of this article.)

seawater) and embedding resin in pores.We know of no Cl-containing mineral likely to be deposited as part of the nodule.We therefore consider this element as a proxy for porosity.The dotted lines in Fig. 2 are drawn to match maxima in the Cl signal.The Fe, Mn and Ce signals have maxima between the bands, showing that all participate in the general density modulation.However, each of the metals has maxima at slightly different places between the bands, so there is not a match between the profiles of Fe, Mn or Ce.

Aside from the “banding” patterns observed in the Ce maps being similar to those of the Fe and Mn maps, there is no obvious match between the Ce distributions to those of either Fe or Mn.From the XRF maps alone, we cannot discern whether Ce is preferentially associated with either of the major elements.We searched for a relationship between the Ce concentrations and those of Fe and Mn by looking for a linear combination of the Fe and Mn images (pixel count values) which would reproduce the Ce image.None were found in any but small areas.

3.2. Cerium spot XANES

Fig. 4 shows examples of Ce XANES taken at two Inner and two Outer spots compared with the XANES of the references.A spread in valence states is obvious.Fig. 5 shows an example of fits to one of the spectra, from an Inner spot.It is clear that even though Ce in CeO_2 is tetravalent as is Ce in δ-MnO_2, the two species are distinct enough so that one needs to use both to describe the spectra from the nodule.

In order to describe the diversity of speciation, we took fluorescence and Ce XANES spectra at 19 spots which were not on the Ce-bright points shown in the maps.We fitted the XANES spectra to our three references and fitted the XRF spectra to Gaussian peaks in order to get

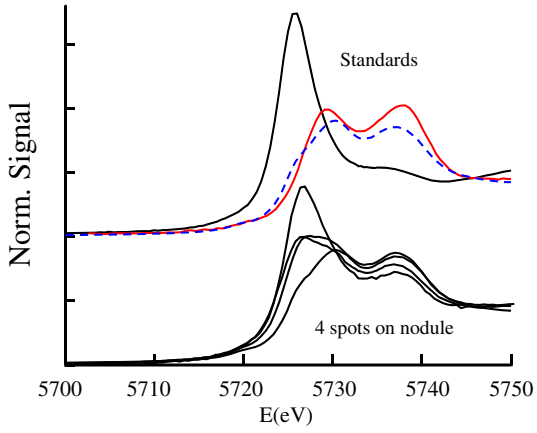

Fig. 4. Representative Ce XANES for four different spots (bottom) compared with references (top; Ce^{3+} on ferrihydrite (black), Ce^{4+} on δ-MnO_2 (red), CeO_2 (blue, dashed). (For interpretation of the references to colour in this figure legend, the reader is referred to the web version of this article.)

relative measures of the Fe/Mn ratios at these spots.Fig. 6 shows the results (tabulated in Supplemental Data Tables 1 and 2), in which the abscissa is not the Fe/Mn molar ratio but the ratio of counts at each spot.We chose the Fe/Mn ratio because these are the major elements and also because Ce is expected to be trivalent when sorbed onto Fe (oxyhydr)oxide and tetravalent on Mn^{4+} oxides (Takahashi et al., 2007). Between the two regions, this expectation is borne out, but within a region, there is no obvious correlation between Fe content and

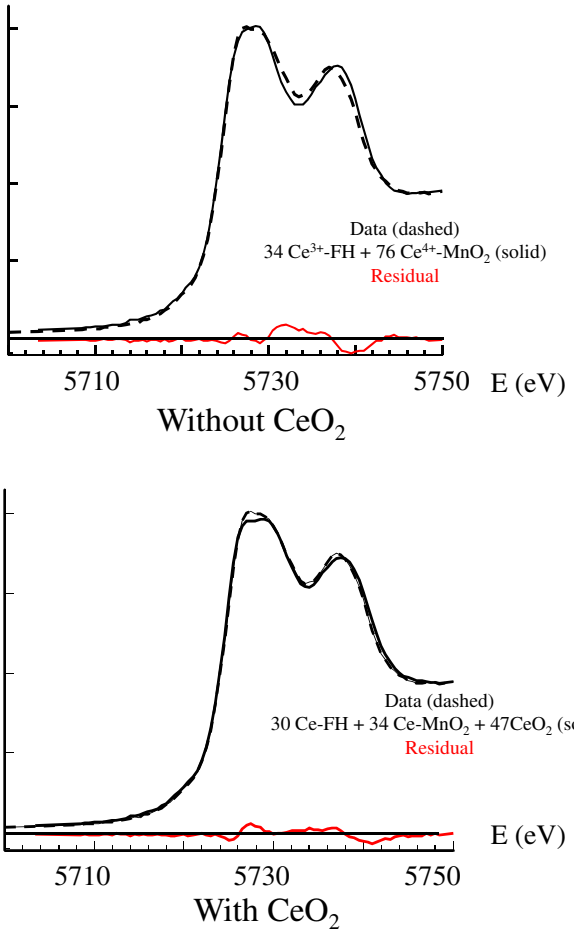

Fig. 5. Example of fits to two and three references.A spot in the inner region (black, dashed) fit (black, solid) to two (top) and three (bottom) species.The fit including CeO_2 is clearly much better than without, as can be seen by the magnitude of the residuals (red). (For interpretation of the references to colour in this figure legend, the reader is referred to the web version of this article.)

valence.For these points, the CeO_2 fraction is less than 20%, so the plot of the fraction of non-CeO_2 Ce^{4+} mirrors that of Ce^{3+}.It should be noted that the areas covered by the 19 spots are small enough so that the entire diversity of the nodule is not represented.A large-area map (e.g. Fig. 3 in (Marcus et al., 2015)) shows a gradual change in Fe-Mn ratio over millimeters, whereas the Inner and Outer subsets of the 19 spots are each less than 1 mm wide.

There are, scattered throughout the nodule, Ca-rich grains of irregular shape and size up to 100 μm.Several of these were examined using an incident energy just below the Ca K-edge and the presence of P was verified in all of them.Calcium XANES was performed on six such spots and the results are consistent with a mixture of fluorapatite and hydroxyapatite in about 2:1 ratio.Due to strong dichroism, it was necessary to fit the XANES to a sum of signals from fluorapatite oriented with the *c*-axis along and perpendicular to the X-ray polarization.We did not have a single crystal of hydroxyapatite on which to do likewise, so we used a powdered specimen.These spots within the apatite grains contain Ce, whose XANES is quite close to that of Ce in the natural sample of fluorapatite described in the Methods section.We measured Ce XANES in four Ca-rich spots (one in Outer, three in Inner).They show differences which could probably be explainable in terms of dichroism.As expected for a trigonal crystal, the XANES spectra could be decomposed into sums of two end-members, and the XANES of our Ce-in-apatite standard fit nicely to a sum of these, consistent with the Ce being contained in single crystals (on the scale of the probe beam) of apatite.

The Ce anomaly in six Ca-rich apatite grains averaged −0.58 with a standard deviation of 0.12.This strongly-negative anomaly suggests an authigenic origin for the apatite, rather than a diagenetic one (Takahashi et al., 2015). The Ce/Ca weight ratio in the apatite standard was 0.023, and on that basis, the Ce/Ca ratio in the nodule apatite was 0.017 with a standard deviation of 0.004.

Cerium XRF maps as shown in Fig. 3 display bright spots.Fig. 7 shows maps in Outer (Fig. 7a) and Inner (Fig. 7b) regions and the Ce speciations derived from linear-combination fitting of XANES spectra to the reference spectra plotted in Fig. 1 of each spot.These compositions are shown on a ternary diagram (Fig. 7c) with sorbed Ce^{4+}, CeO_2 and Ce^{3+} as end-members.In order to make it possible to relate the spot locations to the maps in Fig. 6, we show the Ti signal (which tracks Fe) as red in Fig. 7a,b.Due to the overlap of fluorescence lines between V, Ba and Ti, the “Ti” signal also includes some contribution from the other two elements.The maps shown in these Figures are subsets of the ones in Fig. 6, the difference being that Ce was mapped and bright spots located, whereas in Fig. 6, spot XANES was taken at spots chosen without regard to Ce content. The spots mapped here do not include the Ca-rich grains.We see that the bright spots are variable in composition.The spot XANES results shown in Fig. 7c lie roughly along a line in the ternary diagram, as if the spots were pseudobinary mixtures in which one end-member is sorbed Ce^{4+} and the other is a mixture of Ce^{3+} and CeO_2.

3.3. Chemical-state maps

Point-XANES provides the most chemical accuracy and signal quality achievable, but it does not guarantee representative sampling, nor does it allow us to discover spatial patterns easily (e.g. (Toner et al., 2014)). Chemical-state mapping provides improved representative sampling and has been applied successfully elsewhere for a variety of elements (Heller et al., 2017; Lam et al., 2012; Mayhew et al., 2011; Nicholas et al., 2017; Toner et al., 2012; Zeng et al., 2013). Fig. 8 shows the results of chemical-state mapping on new areas within the petrographic section. While chemical-state mapping in areas with existing XRF and point-XANES would be valuable, we collected the data in areas not extensively exposed to beam to prevent radiation damage and to ensure that preceding point-XANES results are representative.The assignment to Inner and Outer of these two areas is made on the basis of the Fe and Mn maps compared with previous work (Marcus et al., 2015). Note that Fig. 8d shows the presence of an Fe-rich, Mn-poor “matrix” which is devoid of Ce (dark area in Fig. 8b).

As with the Ce point-XANES, we observe Ce in three chemical-states.The bright greenish spots in Fig. 8a and b show varying amounts of CeO_2 when inspected by spot XANES.The blocky red (Ce^{3+}) areas correspond to Ca-rich regions, so are presumably apatite grains.The brightest greenish-white spots in both chemical maps are rich in CeO_2.We plot total Ce^{4+} instead of Ce in MnO_2 as green because the noise in each pixel is less for total Ce^{4+} than for the sorbed species.An interesting trend is observed in the Outer map (Fig. 8a).The botryoidal material contains Ce in oxidation states which vary over broad regions, with a colour gradient from green (oxidized) in the lower left to red (reduced) in the upper right.This gradient is not due to monochromator drift; the calibration was checked using CeO_2 powder before and after the map.Nor would drift produce the horizontal component of the colour gradient because the scan ran from top to bottom.

We could find no consistent relationship between the Fe/Mn ratio and the Ce^{3+}/Ce^{4+} ratio either on a pixel-by-pixel basis or averaged

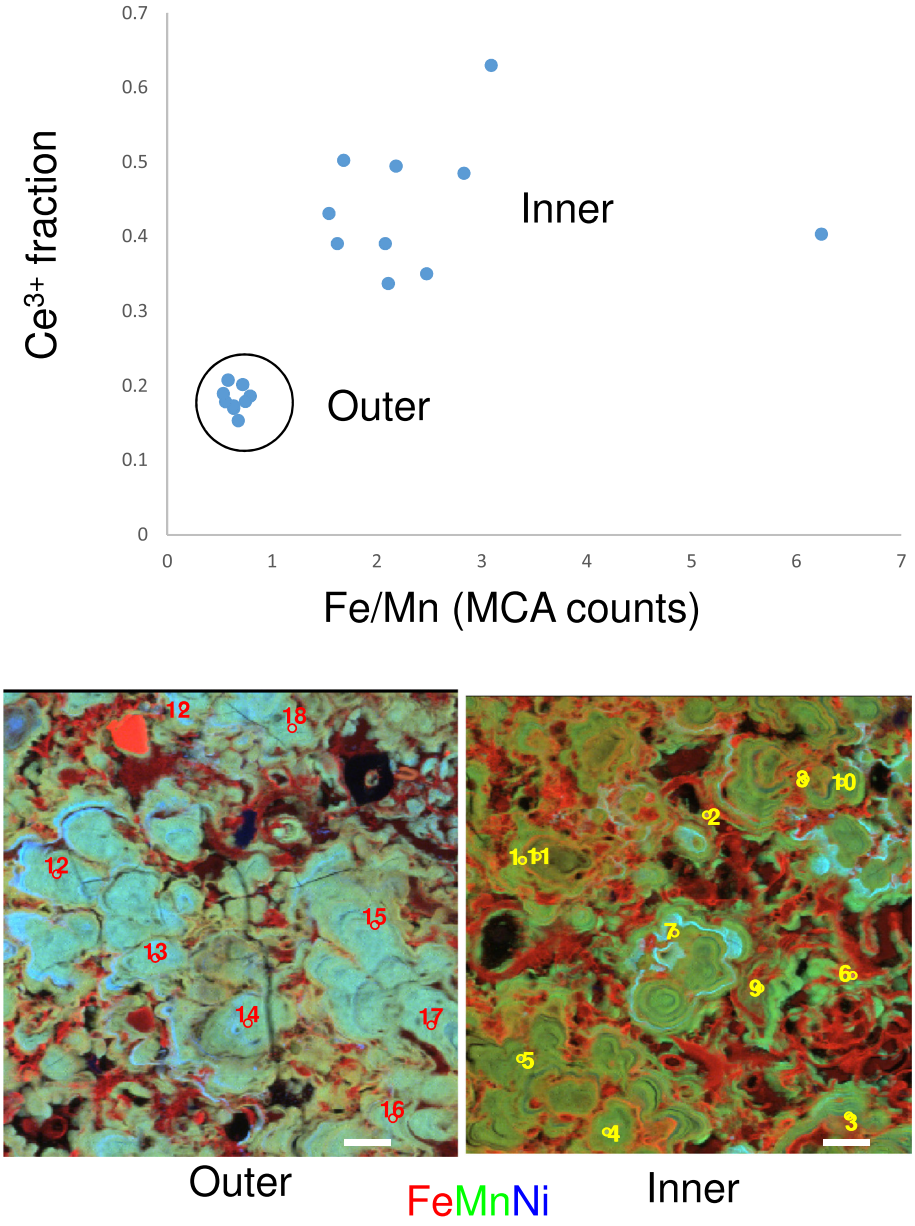

Fig. 6. Results of XANES fitting on 19 spots compared with Fe/Mn count ratios at these spots.The images show the locations at which the spots were taken, with Fe, Mn and Ni coded as red, green and blue.The scalebars are 200 μm long.The Inner map is a superset of the ones in Figs. 2 and 7b, while the Outer map is a superset of the one in Fig. 7a. (For interpretation of the references to colour in this figure legend, the reader is referred to the web version of this article.)

over areas in either chemical map.However, when we masked both maps to remove the matrix (Fe-rich and Mn-poor region; red regions in Fig. 8c and d), the bright Ce^{4+}-rich spots and the Ca-rich spots, we found that the averaged Ce^{3+} fraction was 36% in the Outer map and 43% in the inner, while the Fe/Mn count ratios were 0.33 and 0.63, respectively.Note that these ratios refer in this case to counts in the FeKβ bin, since the FeKα was polluted by the MnKβ.This difference between regions is consistent in sign with that shown in Fig. 6.

4. Discussion

4.1. Cerium reservoirs within the nodule

Fig. 9 summarizes some of the possible processes involved in the incorporation of Ce into the three reservoirs discussed above.This figure is not meant to be a complete set of all possible processes, just the ones which seem likely to have been most important in this nodule.

The “matrix” material has no detectable amount of Ce.The Fe in this material was previously found to be largely in the form of well-crystallized goethite, as opposed to nanoparticulate oxyhydroxides such as ferrihydrite, and is likely to be a product of mineral aging.It seems reasonable to suggest that any Ce which had been associated with young Fe oxyhydroxides of the nodule was expelled during crystallization to goethite.A similar, but much subtler effect was observed for Ti (Marcus et al., 2015). The ionic radius of Ce^{3+} (1.07 Å) is considerably larger than that of Fe^{3+} (0.67 Å), so one would not expect easy substitution of Ce for Fe in crystalline material, whether produced by recrystallization of nanophases such as ferrihydrite or directly as goethite.

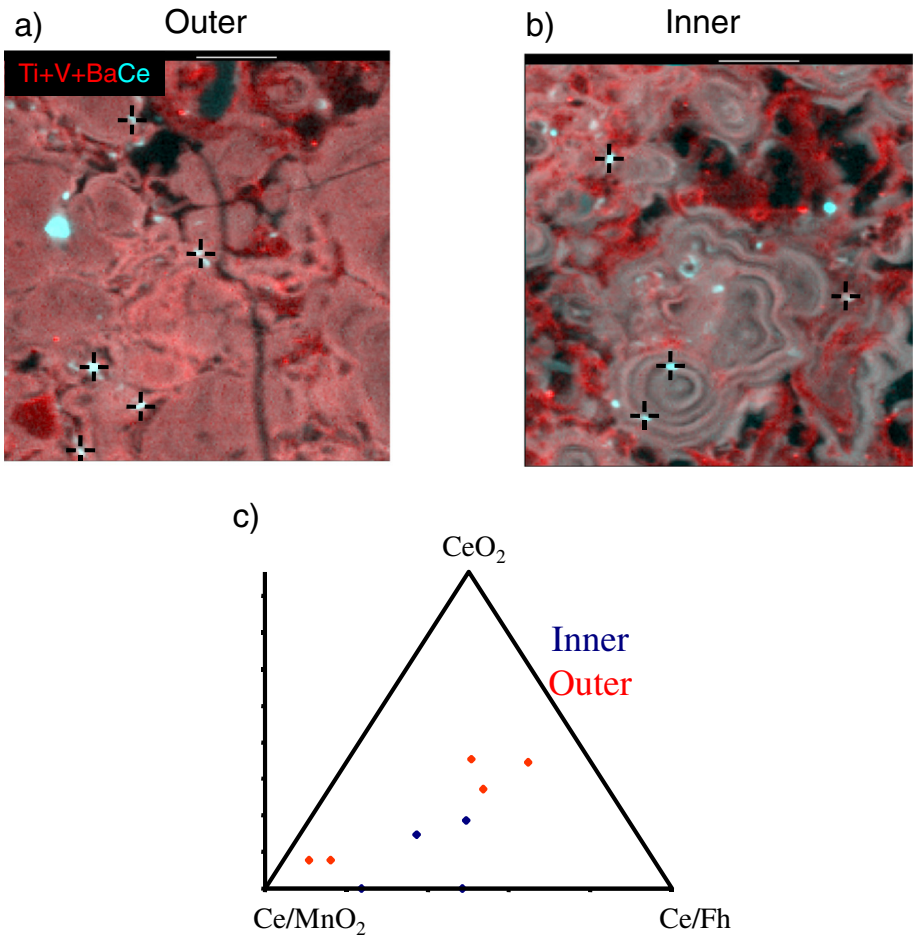

Fig. 7. Bright spots in Outer (a) and Inner (b) regions.Ce is coded as cyan and Ti as red.The Ti signal includes contributions from V and Ba because the fluorescence lines from these elements overlap that of Ti.Since Ti and V follow Fe closely, these elements serve as a proxy for Fe.The scalebar is 200 μm long.The fitted compositions of the spots are shown on a ternary diagram (c) with the Ce^{4+} (modeled as the Ce-on-MnO_2 reference, labeled as Ce/MnO_2), CeO_2 and Ce^{3+} (modeled as the Ce-on-ferrihydrite reference, labeled as Ce/Fh) as end-members. (For interpretation of the references to colour in this figure legend, the reader is referred to the web version of this article.)

We see that there are three reservoirs of Ce in the nodule, one in apatite, one in the bright, oxidized spots, and the majority found everywhere in the botryoidal material in Fig. 8.For purposes of geochemical inference from bulk Ce levels, the first two pools are likely to be of small consequence, judging from the small areas they occupy in the maps.However, the presence of the Ce-poor matrix (red regions in Fig. 8c and d) may pull down the averaged Ce abundance in bulk measurements, assuming that other nodules have similar Ce distributions to ours.A way around this problem for future studies might be to report the REE/Mn ratios, as the matrix is nearly devoid of Mn.We do not know at this point whether the matrix is similarly devoid of other REE.If it is, then measurements of the Ce anomaly would be unaffected by the matrix.

The apatite resembles terrestrial apatite in that it is mostly fluorapatite and contains significant levels of Ce.However, the negative Ce anomaly suggests an authigenic origin rather than a terrestrial one.By comparison, our geologic sample has a low Ce anomaly value of +0.042.Because the apatite is found as large lumps at long distances from each other, it is difficult to measure reliably the fraction of Ce that is carried in the apatite.However, in the map in Fig. 8, about 0.8% of the total Ce is contained within Ca-rich spots.Thus, it is likely that the contribution of the apatite reservoir to the total Ce content is small.However, due to the localized nature of the apatite, this contribution is easily detected.

The bright spots occur in places that do not seem to correlate with any obvious features of morphology, as seen in Fig. 7, whereas Fig. 8 demonstrates that some occur in places where there is a break in the growth (Outer) or at the boundary between matrix and botryoid.These patterns are consistent with particles of Ce-rich material either falling out of the water column or being formed on the surface during growth.One of the known mechanisms for the formation of cerianite is the oxidation of dissolved Ce^{3+} to CeO_2 (Braun et al., 1990). Perhaps Ce^{3+} in the nodule was associated with carbonate minerals such as dolomite (Schijf et al., 1995) which dissolved after incorporation into the nodule. A process such as this would release Ce that could be oxidized and deposited within the nodule.Another possible source for cerianite is the formation of particles in the water column, which then adhered to the growing nodule.Since the nodule was collected from an oxic region of the Pacific (see Fig. 5 in (Molina-Kescher et al., 2014)), it is plausible that any Ce^{3+} in the water column would be oxidized to CeO_2 (s) and precipitate as particles (Brookins, 1983; Schijf et al., 1995) that settle and adhere to the nodule.However, neither of these ideas explain why the “end-member” in the ternary diagram of Fig. 8 is a mixture of CeO_2 and Ce^{3+}. A possible scenario which would account for this observation is that Ce in the water column was incorporated, either as aqueous Ce^{4+} species or CeO_2 particles, into solids rich in organic matter such as zooplankton (Byrne and Kim, 1990; Fisher et al., 1991; Schijf et al., 1995), and then partially reduced during settling or at the seafloor by the lower redox conditions supported by the organic matter.

Since the oxidation rate of Ce^{3+} to Ce^{4+} on MnO_2 seems to be much faster than that of Ce^{3+} by dissolved oxygen in aqueous phase (e.g. (Nakada et al., 2013), the presence of MnO_2 in the dissolved Ce^{3+} system produces Ce^{4+} sorbed on MnO_2.This argument agrees with that

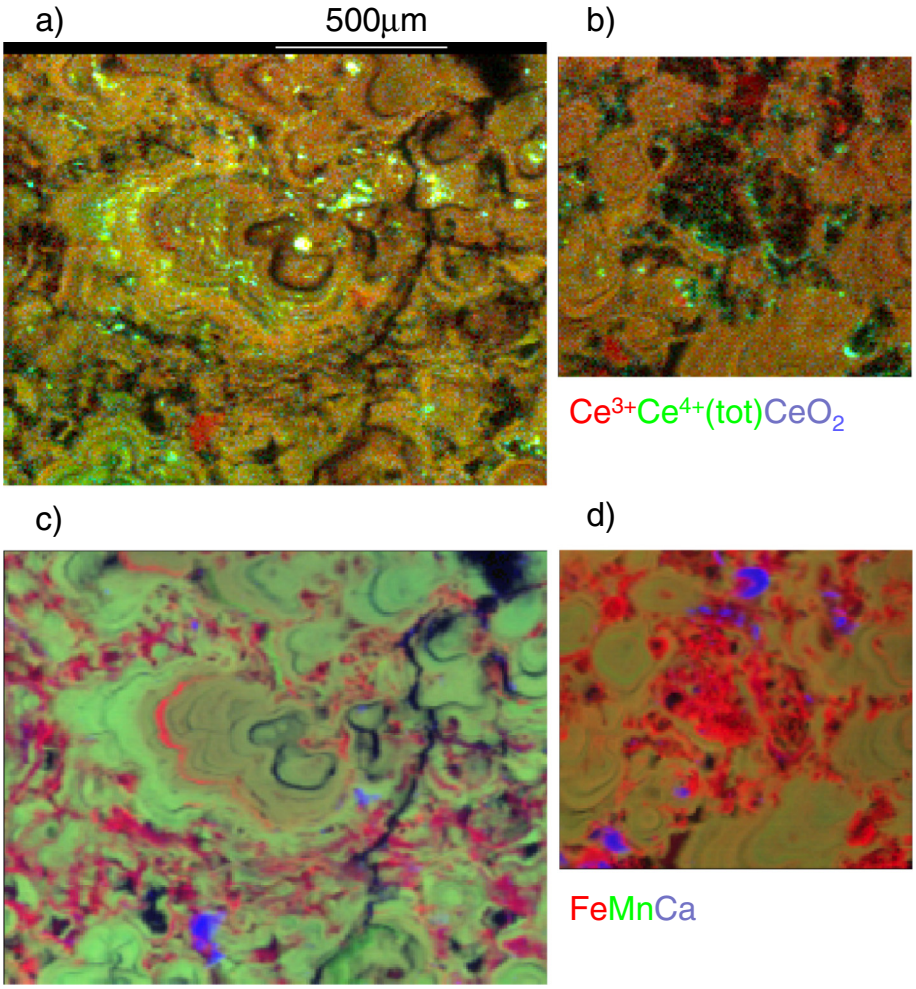

Fig. 8. A,b: Chemical-state maps for Outer (a) and Inner (b) with Ce^{3+}, total Ce^{4+} (Ce-MnO_2 + CeO_2) and CeO_2 coded in red, green and blue, respectively.The white levels for these three channels are in the ratio of 3:6.8:9.C,d: Elemental maps of the same areas showing Fe in red, Mn and green and Ca in blue, with the white levels for Fe and Mn in the same ratio in d) as in c). (For interpretation of the references to colour in this figure legend, the reader is referred to the web version of this article.)

given by (Bau and Koschinsky, 2009) whose sequential-extraction study of crusts also suggest that Ce^{3+} is mainly oxidized by the solid phase.

Finally, the weak correlation between valence state and Fe/Mn ratio within a region (Inner/Outer) suggests either that the Ce was deposited with redox state depending on changing environmental variables or that it came in as, for instance, MnO_2-sorbed Ce^{4+} and was altered later.The greater Ce^{3+} fraction seen in the older, Inner material would be consistent with a picture of initial deposition as Ce^{4+} followed by reduction.However, the presence of cerianite suggests traffic in the opposite direction, with Ce^{3+} being oxidized.Similarly, if the Ce were initially sorbed as Ce^{3+} on ferrihydrite, it might have found its way to nearby Mn oxides and sorbed there, with oxidation.

5. Conclusions

To summarize, we have found Ce in three environments, each with its own redox state and each with its own history.The inhomogeneity of Ce concentration suggests that caution must be applied in the use of whole-nodule chemical analyses. For example, the Fe-rich “matrix” is almost devoid of Ce.The presence of Ce^{3+} in the botryoidal material, especially in the Inner region, would seem to point to a reduction process, while the occurrence of CeO_2 shows that oxic alteration must have happened at some point.The negative Ce anomaly found in apatite grains shows that these are neither from terrestrial sources nor from diagenetic processes.As we previously found for Fe (Marcus et al., 2015), the speciation of Ce is diverse and encodes information about the geochemical history of the host nodule.

As argued above, Ce^{3+} in the nodule is likely to have oxidized as sorbed Ce^{4+}. Thus, observation of CeO_2 in the nodule reveals that Ce was also oxidized within the water column, which was finally adhered to MnO_2. Since this species was found mostly in localized spots using X-ray microprobe, it is difficult to estimate its overall abundance, but it seems likely to be present in quantity too small to affect bulk results such as those of (Bau and Koschinsky, 2009). This fact in turn suggests that the Ce within the ferromanganese nodule is a mixture of materials of two origins: one is produced within the water column, while the other is formed by growing at the surface of ferromanganese oxides including adsorption reactions of various ions.

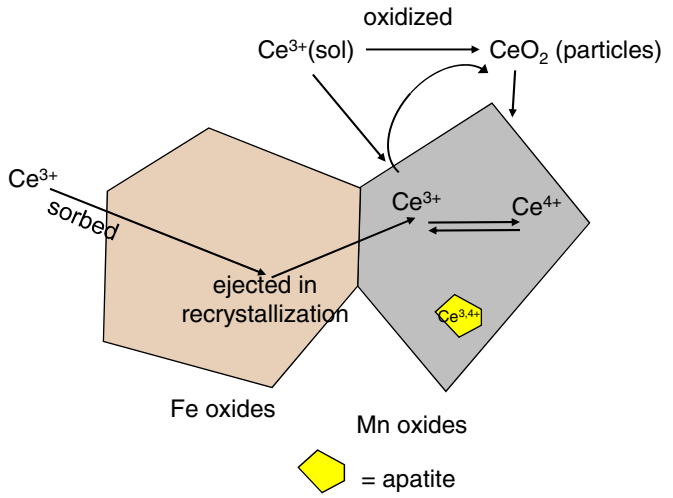

Fig. 9. Schematic showing some of the processes by which Ce may be transported between the nodule and seawater, and its chemistry altered.The yellow polygon represents a crystal of apatite, with the Ce it incorporated during growth.The larger polygons represent the nanostructured Fe oxyhydroxides and Mn oxides which form the bulk of the nodule, and the background represents the ambient seawater.The processes depicted are those described in the Discussion and Conclusion sections and are not intended to be a complete set of all possible processes. (For interpretation of the references to colour in this figure legend, the reader is referred to the web version of this article.)

Acknowledgements

We thank the science team, especially Gregory Horn, the crew, and the Chief Scientist Steven D'Hondt of the KNOX02RR cruise for access to the South Pacific Gyre nodule samples. We gratefully acknowledge John Fournelle and Tony Giuffre for sample preparation and electron microprobe on the apatite standard. The Advanced Light Source is supported by the Director, Office of Science, Office of Basic Energy Sciences, of the U.S. Department of Energy under Contract No. DEAC02-05CH11231.

Appendix A. Supplementary data

Supplementary data to this article can be found online at https://doi.org/10.1016/j.marchem.2018.03.005.

References

Anders, E., Grevesse, N., 1989. Abundances of the elements: meteoritic and solar. Geochim. Cosmochim. Acta 53 (1), 197–214.
De Baar, H., Schijf, J., Byrne, R., 1991. Solution chemistry of the rare earth elements in seawater. Eur. J. Solid State Inorg. Chem. 28 (Suppl. S), 357–373.
Bau, M., Koschinsky, A., 2009. Oxidative scavenging of cerium on hydrous Fe oxide: evidence from the distribution of rare earth elements and yttrium between Fe oxides and Mn oxides in hydrogenetic ferromanganese crusts. Geochem. J. 43 (1), 37–47.
Bau, M., et al., 2014. Discriminating between different genetic types of marine ferromanganese crusts and nodules based on rare earth elements and yttrium. Chem. Geol. 381, 1–9.
Braun, J.-J., et al., 1990. Cerium anomalies in lateritic profiles. Geochim. Cosmochim. Acta 54 (3), 781–795.
Brookins, D.G., 1983. Eh-pH diagrams for the rare earth elements at 25 C and one bar pressure. Geochem. J. 17 (5), 223–229.
Byrne, R.H., Kim, K.-H., 1990. Rare earth element scavenging in seawater. Geochim. Cosmochim. Acta 54 (10), 2645–2656.
Calvert, S.E., Cronan, D.S., 1978. Geochemistry of oceanic ferromanganese deposits. Philos. Trans. R. Soc. Lond. A 290, 43–73.
Elderfield, H., Whitfield, M., Burton, J., Bacon, M., Liss, P., 1988. The oceanic chemistry of the rare-earth elements [and discussion]. Philos. Trans. R. Soc. Lond. A 325 (1583), 105–126.
Fisher, N.S., Nolan, C.V., Fowler, S.W., 1991. Scavenging and retention of metals by zooplankton fecal pellets and marine snow. Deep Sea Res. A. Oceanogr. Res. Papers 38 (10), 1261–1275.
Gradstein, F., Ogg, J., 2002. Future directions in stratigraphy. Episodes 25 (3), 203–208.
Hein, J.R., Mizell, K., Koschinsky, A., Conrad, T.A., 2013. Deep-ocean mineral deposits as a source of critical metals for high-and green-technology applications: comparison with land-based resources. Ore Geol. Rev. 51, 1–14.
Heller, M.I., et al., 2017. Accumulation of Fe oxyhydroxides in the Peruvian oxygen deficient zone implies non-oxygen dependent Fe oxidation. Geochim. Cosmochim. Acta 211, 174–193.
Kaindl, G., Schmiester, G., Sampathkumaran, E., Wachter, P., 1988. Pressure-induced changes in L III X-ray-absorption near-edge structure of Ce O_2 and Ce F_4: relevance to 4 f-electronic structure. Phys. Rev. B 38 (14), 10174.
Koschinsky, A., Hein, J.R., 2003. Uptake of elements from seawater by ferromanganese crusts: solid-phase associations and seawater speciation. Mar. Geol. 198, 331–351.
Lam, P.J., Ohnemus, D.C., Marcus, M.A., 2012. The speciation of marine particulate iron adjacent to active and passive continental margins. Geochim. Cosmochim. Acta 80, 108–124.
Larson, R.L., et al., 2002. Mid-cretaceous tectonic evolution of the Tongareva triple junction in the southwestern Pacific Basin. Geology 30 (1), 67–70.
Manceau, A., et al., 2002. Deciphering Ni sequestration in soil ferromanganese nodules by combining X-ray fluorescence, absorption, and diffraction at micrometer scales of resolution. Am. Mineral. 87 (10), 1494–1499.
Marcus, M.A., Manceau, A., Kersten, M., 2004. Mn, Fe, Zn and As speciation in a fast-growing ferromanganese marine nodule. Geochim. Cosmochim. Acta 68 (14), 3125–3136.
Marcus, M.A., et al., 2015. Iron mineral structure, reactivity, and isotopic composition in a South Pacific gyre ferromanganese nodule over 4Ma. Geochim. Cosmochim. Acta 171, 61–79.
Mayhew, L., Webb, S., Templeton, A., 2011. Microscale imaging and identification of Fe oxidation state, speciation, and distribution in complex geological media. Environ. Sci. Technol. 45, 4468–4472.
Molina-Kescher, M., Frank, M., Hathorne, E., 2014. South Pacific dissolved Nd isotope compositions and rare earth element distributions: water mass mixing versus biogeochemical cycling. Geochim. Cosmochim. Acta 127, 171–189.
Nakada, R., Takahashi, Y., Tanimizu, M., 2013. Isotopic and speciation study on cerium during its solid–water distribution with implication for Ce stable isotope as a paleo-redox proxy. Geochim. Cosmochim. Acta 103, 49–62.
Nicholas, S.L., et al., 2017. Solid-phase arsenic speciation in aquifer sediments: a micro-X-ray absorption spectroscopy approach for quantifying trace-level speciation. Geochim. Cosmochim. Acta 211, 228–255.
Peacock, C.L., Sherman, D.M., 2007. Crystal-chemistry of Ni in marine ferromanganese crusts and nodules. Am. Mineral. 92 (7), 1087–1092.
Schijf, J., De Baar, H.J., Millero, F.J., 1995. Vertical distributions and speciation of dissolved rare earth elements in the anoxic brines of Bannock Basin, eastern Mediterranean Sea. Geochim. Cosmochim. Acta 59 (16), 3285–3299.
Soldatov, A., et al., 1994. Crystal-structure effects in the Ce L_3-edge x-ray-absorption spectrum of CeO_2: multiple-scattering resonances and many-body final states. Phys. Rev. B 50 (8), 5074.
Takahashi, Y., Shimizu, H., Usui, A., Kagi, H., Nomura, M., 2000. Direct observation of tetravalent cerium in ferromanganese nodules and crusts by X-ray-absorption near-edge structure (XANES). Geochim. Cosmochim. Acta 64 (17), 2929–2935.
Takahashi, Y., Sakami, H., Nomura, M., 2002. Determination of the oxidation state of cerium in rocks by Ce L III-edge X-ray absorption near-edge structure spectroscopy. Anal. Chim. Acta 468 (2), 345–354.
Takahashi, Y., Manceau, A., Geoffroy, N., Marcus, M.A., Usui, A., 2007. Chemical and structural control of the partitioning of Co, Ce, and Pb in marine ferromanganese oxides. Geochim. Cosmochim. Acta 71 (4), 984–1008.
Takahashi, Y., et al., 2015. Transfer of rare earth elements (REE) from manganese oxides to phosphates during early diagenesis in pelagic sediments inferred from REE patterns, X-ray absorption spectroscopy, and chemical leaching method. Geochem. J. 49 (6), 653–674.
Toner, B., et al., 2012. Mineralogy of iron microbial mats from Loihi seamount. Front. Microbiol. 3 (118).
Toner, B.M., Nicholas, S.L., Wasik, J.K.C., 2014. Scaling up: fulfilling the promise of X-ray microprobe for biogeochemical research. Environ. Chem. 11 (1), 4–9.
Toner, B.M., Rouxel, O.J., Santelli, C.M., Bach, W., Edwards, K.J., 2016. Iron transformation pathways and redox micro-environments in seafloor sulfide-mineral deposits: spatially resolved Fe XAS and $\delta^{57}/^{54}$Fe observations. Front. Microbiol. 7 (648).
Yang, Y.-H., et al., 2014. Sr and Nd isotopic compositions of apatite reference materials used in U–Th–Pb geochronology. Chem. Geol. 385, 35–55.
Zeng, T., Arnold, W.A., Toner, B.M., 2013. Microscale characterization of sulfur speciation in lake sediments. Environ. Sci. Technol. 47 (3), 1287–1296.